The International Journal of Advanced Manufacturing Technology (2023) 128:5261–5276
https://doi.org/10.1007/s00170-023-12220-4

ORIGINAL ARTICLE

Interelectrode gas–liquid-solid three-phase flow analysis and simulation for drilling holes with high aspect ratio by micro-EDM

Peiyao Cao[1,2] · Hao Tong[1,2] · Yong Li[1,2] · Jialong Chen[1,2]

Received: 6 October 2022 / Accepted: 23 August 2023 / Published online: 7 September 2023

Abstract
In micro-electrical discharge machining (micro-EDM) using the non-hollow circular cross-section tool electrode with the side flushing technique, when the aspect ratio of machined micro-hole is expected to be further increased, the discharge debris expelling speed and the working fluid renewal efficiency are weakened, which hinders the improvement of machining efficiency and accuracy with increased machining depth. In order to reveal the flow behavior of the working fluid in the micro-EDM gap, so as to realize the high-precision and high-efficiency machining of micro-hole with high aspect ratio, a three-phase flow simulation model of fluid, bubble, and debris is established in Fluent under the ideal assumption that the spark discharges occur continuously to generate high-pressure bubbles. The simulation results show that when the boundary condition of the flushing pressure at the side gap entrance is set to 0, the pressure wave emitted when the high-pressure bubble expands, which is formed by the instantaneous gasification of the working fluid between electrodes under high temperature, is the source of pneumatic force that drives the working fluid flow at the micron scale. Affected by the gap flow channel structure and the viscous resistance from inner wall, the flow velocity direction of the fluid dragging the discharge debris to rise up and expel will change, forming a dynamic alternation process of flowing into and out of the side machining gap entry. As the machining depth increases, due to the energy attenuation of the pressure wave propagating from the bottom gap to the side gap entrance, the expelling speed of the discharge debris decreases exponentially at the side gap entrance, resulting in the reduced machining efficiency and accuracy. However, when the simulated bubble generation frequency is increased to the megahertz level, the expelling efficiency of debris has a step-like improvement. The continuous and high-frequency generation of high-pressure bubbles can maintain a high pressure gradient in the bottom gap, and the discharge debris is able to continuously move upward without falling back to accumulate in the bottom gap, which is beneficial to the stable and smooth machining process, realizing the high-precision and high-efficiency machining of micro-hole with high aspect ratio.

Keywords Micro-EDM · Micro-hole · High aspect ratio · Flow simulation · Bubble · Debris

1 Introduction

With the rapid development of advanced manufacturing technology and the intensification of competition in the manufacturing market, products tend to be miniaturized, micro-sized, and precision-oriented, and the requirements for machining accuracy are becoming increasingly higher. The application demand for micro-hole structural components is showing a significant growth trend in fields such as vehicles, biomedical, precision instruments, micro-parts and molds, and aerospace [1–3].

EDM is one of the effective methods for micro-hole machining. When the diameter of machined micro-hole is less than about 200 μm, the EDM process transits to micro-machining scale, and the general flushing method of the hollow tool electrode with internal flushing to remove the discharge debris is no longer applicable. The micro-EDM process often uses the drawing technique or the online WEDG to fabricate micro-electrodes, and the solid micro-electrodes with circular cross-section are economically applicable [4]. In micro-hole EDM process using the solid

✉ Yong Li
liyong@mail.tsinghua.edu.cn

1 State Key Laboratory of Tribology in Advanced Equipment, Department of Mechanical Engineering, Tsinghua University, Beijing 100084, China

2 Beijing Key Lab of Precision/Ultra-Precision Manufacturing Equipment and Control, Tsinghua University, Beijing 100084, China

micro-electrodes with circular cross-section, the interelectrode dielectric condition, namely, the inflow of fresh working fluid and the outflow of discharge debris, has a significant impact on the smooth progress of machining.

Additional rotation or vibration of the electrode is conducive to the normal progress of the micro-EDM process. The rotation of the tool electrode drives the circulating flow of the working fluid through the viscous resistance exerted to the working fluid from the rough wall of the tool electrode [5, 6]. The auxiliary high-frequency vibration of electrodes can promote the circulation of the working medium through a pumping effect [7]. On the other hand, the size of the side machining gap in micro-EDM is small, and the effect of the commonly used external flushing decreases rapidly with the machining depth. Li and Natsu [8] designed a high-pressure vertical flushing device to avoid the deflection and vibration of the tool electrode caused by unbalanced forces exerted on both sides of the tool electrode. Liao and Liang [9] adopted the method of inverted workpiece and inclined feeding tool electrode to promote the outflow of debris.

The experimental results of micro-hole EDM process show that generally, when the machining aspect ratio is less than or equal to 5:1, the machining efficiency and the dimensional consistency are preferable. With the above-mentioned techniques of working fluid renewal and discharge debris expelling, the micro-hole with an aspect ratio of 10:1 can be machined in a certain machining efficiency and accuracy. However, if the aspect ratio of micro-hole is expected to be further increased with acceptable machining efficiency and accuracy, a technical bottleneck is encountered.

Preliminary experimental studies have found that the micro-hole machined by EDM generally appears to have a “waist drum” shape with a large diameter in the middle and small diameters at both ends [10]. The reason is that when the machining depth reaches a certain value, due to the poor debris removal efficiency, the lateral secondary discharge occurs between the tool electrode and debris, which leads to the reduction of machining efficiency and accuracy. In the actual machining experiments, it is also observed that the process is smooth at certain machining depth. At this time, the working fluid at the exit of the machining gap is mixed with not only discharge debris but also the generated bubbles.

According to the experimental phenomena, it can be reasonably assumed that the working fluid in the machining gap is a gas–liquid-solid three-phase flow, which leads to more in-depth thinking: while the high temperature produced from the instantaneous discharges gasifies the working fluid to form high-pressure bubbles, the high-pressure bubbles may exert pneumatic force to drive the working fluid flow at the micron scale.

Li et al. [11] used the transparent SiC plate to directly observe the expansion and contraction process of bubbles generated by single-pulse discharge in micro-EDM. They found that the continuous accumulation of gas-phase volume resulted from the longer time required for bubble contraction than expansion, and bubbles tended to stay in the gap when the machining depth reached a certain value, which led to spark discharges in gas medium. Yin et al. [12] used the weak conductive solution as the working fluid so that the spark discharge process was accompanied by the electrochemical reaction. A large number of hydrogen and oxygen bubbles were generated, and the micro-hole with high aspect ratio and high dimensional accuracy was obtained.

EDM is a process influenced by many factors. In addition to the materials of electrodes, the pulsed power supply, and the servo control of the machining gap, the most critical factors are the expelling of discharge debris and the renewal of working fluid. This requires a deep understanding of the discharge erosion process and the three-phase flow mechanism in the machining gap, so as to derive a feasible technical path for high-precision and high-efficiency machining of micro-holes with high aspect ratio.

This study focuses on the flow of the working fluid between electrodes and simplifies the effect of the plasma discharge channel on the surrounding working fluid into generating instantaneous high-temperature and high-pressure bubbles. The characteristics of gap flow field in micro-EDM are analyzed from the perspective of computational fluid dynamics. Under the ideal assumption that the spark discharges occur continuously to constantly generate bubbles, the models of fluid, bubble, and debris are respectively established in the software Fluent. Based on the calculation results of the pressure loss of flushing along the narrow machining gap, the boundary condition of the entrance pressure at the side gap is set to 0, so as to reveal the influencing factors and characteristics of the gap flow. As the basic research on the flow mechanism, the phenomenon of bubble stagnation in the machining gap under the micro-scale effect is studied. Meanwhile, the influence of the pressure waves emitted by the expansion and contraction of bubbles on the pressure and velocity distribution of the surrounding working fluid is analyzed, which explains the driving force source to expel the discharge debris. A special phenomenon of the dynamic alternation process of the working fluid flowing into and out of the side machining gap entry is discovered, which reveals the nature of the working fluid circulation. In addition, the influence trend of different bubble generation frequencies on the debris removal efficiency is studied. Verification experiments are conducted in the final section.

2 Simulation model

The Volume of Fluid (VOF) model in Fluent, which is able to simulate two-phase immiscible fluid, is used to simulate the movement of bubbles in the dielectric fluid. Combined with the Discrete Phase Model (DPM) in Fluent, which can simulate the movement of discrete-phase debris in the flow field, the gas–liquid-solid three-phase simulation is realizable. Considering that the interelectrode micron-scale gap in micro-EDM causes a large loss of flushing pressure, the reason for setting the flushing pressure in boundary conditions to the atmospheric pressure is analyzed through numerical calculation in Section 2.4.

2.1 Model of fluid

The continuity Eq. (1) containing the volume fractions of p-phase α_p and q-phase α_q is solved in the VOF model to track the moving interface between liquid phase and gas phase, and thus, the shape change of bubbles is captured [13]:

$$\frac{1}{\rho_q}\frac{\partial\left(\alpha_q\rho_q\right)}{\partial t}+\frac{1}{\rho_q}\bullet\nabla\left(\alpha_q\rho_q v_q\right)=\frac{S_{\alpha_q}}{\rho_q}+\frac{1}{\rho_q}\sum_{p=1}^{n}\left(\dot{m}_{pq}-\dot{m}_{qp}\right) \tag{1}$$

where $\alpha_\mathrm{p}+\alpha_\mathrm{q}=1$. The materials of p-phase and q-phase are designated as water-liquid and water–vapor respectively, in order to simulate the process of the deionized water as dielectric fluid gasified under high temperature to generate high-pressure bubbles. The property of water-liquid is set to compressible so that the effect of gas-phase pressure change on the surrounding liquid-phase flow velocity is taken into account [14], though the compression factor of water-liquid is as small as 0.0485 m^2/N. The Euler implicit scheme is used to discretize the continuity Eq. (1), which allows observation and analysis of the entire movement process of bubbles rather than a final state. The volume fraction of q-phase at the $n+1$ time step $\alpha_\mathrm{q}^{\mathrm{n}+1}$ is iteratively solved by that at the n time step $\alpha_\mathrm{q}^{\mathrm{n}}$:

$$\frac{\alpha_q^{n+1}\rho_q^{n+1}-\alpha_q^n\rho_q^n}{\Delta t}V_c+\sum_f\left(\rho_q^{n+1}V_f^{n+1}\alpha_q^{n+1}\right)=\left[S_{\alpha_q}+\sum_{p=1}^{n}\left(\dot{m}_{pq}-\dot{m}_{qp}\right)\right]V_c \tag{2}$$

The momentum Eq. (3) is solved where the value of each variable is shared by different phases:

$$\frac{\partial(\rho v)}{\partial t}+\nabla\bullet(\rho v v)=-\nabla p+\nabla\bullet\left[\mu\left(\nabla v+\nabla v^T\right)\right]+\rho g+F_\sigma \tag{3}$$

Equation (3) includes the effect of surface tension: $F_\sigma=\sigma\kappa n_v$, where the surface tension coefficient σ is 0.0728 N/m.

The process of dielectric fluid absorbing heat from the discharge channel and generating bubbles involves heat transfer and mass transfer. Therefore, the energy Eq. (4) is used to simulate the actual physical process and improve the solution accuracy:

$$\frac{\partial}{\partial t}\left(\rho E_e\right)+\nabla\bullet\left(v\left(\rho E_e+p\right)\right)=\nabla\bullet\left(k_{\mathrm{eff}}\nabla T_e\right)+S_h \tag{4}$$

where the mass transfer mechanism of the source term S_h is set as evaporation–condensation, which can imitate the evaporation of dielectric fluid and the condensation of bubbles. S_h is equal to $\dot{\mathrm{m}}_{\mathrm{pq}}\mathrm{L}_\mathrm{e}$ when liquid p-phase evaporates into gas q-phase, while S_h is equal to $-\dot{\mathrm{m}}_{\mathrm{qp}}\mathrm{L}_\mathrm{e}$ when gas q-phase condenses into liquid p-phase. Among them, the mass transfer rate $\dot{\mathrm{m}}_{\mathrm{qp}}$ is calculated using the Lee model:

$$\dot{\mathrm{m}}_{\mathrm{qp}}=\mathrm{K}_{\mathrm{qp}}\alpha_\mathrm{q}\left(\mathrm{p}_\mathrm{q}-\mathrm{p}_{\mathrm{sat}}\right) \tag{5}$$

where the initial value of saturated vapor pressure p_{sat} is assigned 4 kPa ($\mathrm{T}_{\mathrm{sat}}=303\mathrm{K}$), and in subsequent time steps, the program will automatically reassign p_{sat} according to the temperature calculated in real time.

The viscous model is determined through calculating the Reynolds number of the fluid in bottom and side machining gaps respectively. The Reynolds number of the fluid in bottom machining gap is calculated in Eq. (6):

$$\mathrm{Re}_\mathrm{b}=\frac{\mathrm{v}_\mathrm{b}\mathrm{l}_\mathrm{g}}{\upsilon} \tag{6}$$

where the initial bubble expansion velocity v_b is 10 m/s [15], the machining gap width l_g in micro-EDM is 10 μm, and the kinematic viscosity υ of deionized water is $1\times10^{-6}\mathrm{m}^2/\mathrm{s}$. As a result, $\mathrm{Re}_\mathrm{b}=100<2300$, which signifies the laminar flow regime of fluid in bottom machining gap. Similarly, the Reynolds number of the fluid in side machining gap is estimated in Eq. (7):

$$\mathrm{Re}_\mathrm{s}=\frac{\mathrm{v}_\mathrm{s}\mathrm{d}_\mathrm{e}}{\upsilon} \tag{7}$$

Due to the kinetic energy loss from the viscous resistance of fluid, the flow velocity v_s in the side machining gap is much smaller than the initial bubble expansion velocity v_b in the bottom machining gap. The cross-section of the side machining gap along the electrode diameter direction can be simplified as a ring, whose equivalent diameter $\mathrm{d}_\mathrm{e}=\frac{4A_S}{\chi}=20\mu\mathrm{m}$, where the flow area $A_S=\frac{\pi d_2^2}{4}-\frac{\pi d_1^2}{4}$ and the wetted perimeter $\chi=\pi d_1+\pi d_2$. As a result, $\mathrm{Re}_\mathrm{s}<\mathrm{Re}_\mathrm{b}<2300$, which signifies the identical laminar flow regime of fluid also in side machining gap.

2.2 Model of bubble

The requisite thermal energy for liquid gasification to generate bubbles is derived from the electrical energy of the pulsed power supply, which can be calculated by the Gaussian heat source model [16]:

$$q(r,t) = \frac{k_G}{\pi R^2(t)} U(t) I(t) \eta_G \bullet e^{-k_G \frac{r^2}{R^2(t)}} \tag{8}$$

where the empirical formula for calculating the discharge channel radius is $R(t) = 1.2 \bullet 10^{-3} \bullet I(t)^{0.43} \bullet t_{on}^{0.44}$. The smaller distance from discharge center r means the larger Gaussian heat $q(r,t)$. This Gaussian heat is transferred to the liquid to boil, forming the gas nucleus [17], whose initial radius r_{bi} is estimated through Eq. (9):

$$\mathrm{r_{bi}} = \frac{2\sigma \mathrm{T_{sat}}}{(\mathrm{T_{nuc}} - \mathrm{T_{sat}})\rho_q \mathrm{h_v}} \tag{9}$$

where $\mathrm{r_{bi}} = 5\mu\mathrm{m}$ as the initial radius of generated spherical bubbles. The instantaneous gasification process of liquid results in much larger internal pressure of generated bubbles than the pressure of surrounding liquid. Therefore, the initial pressure inside bubbles is set to 200 MPa [18] through the user-defined function (UDF).

In the actual machining process, one macroscopic discharge process observed from an oscilloscope contains several synchronous discharges at different locations on the electrode surface, generating several bubbles at the same time [19]. Therefore, the number of discharges per unit time is determined by calculating the material removal rate (MRR) of workpiece; then, the number and time interval of bubble generation are confirmed:

$$\overline{\mathrm{MRR}} = \frac{\mathrm{V_{total}}}{\mathrm{t_{total}}} = \frac{\Delta V}{\Delta t} = \mathrm{MRR(t)} \tag{10}$$

where the MRR of entire machining process $\overline{MRR}$ is assumed to be equal to the MRR over a period of time MRR(t); that is, the machining process is considered to be smooth and uniform. During the unit time Δt, the material removal volume ΔV is deemed to be equal to the number of discharges N multiplied by the volume of a single discharge crater V_{crater}, which is simplified as a hemisphere for calculation: $\mathrm{V_{crater}} = \frac{2}{3}\pi \mathrm{R(t)}^3$. When substituting the variable with the actual value of micro-EDM at low efficiency: $\overline{\mathrm{MRR}} = 7.85 \times 10^{-12} \mathrm{m^3/s}$, the number of discharges N reaches 4 per 2.5×10^{-5}s, while when substituting the variable at high efficiency: $\overline{\mathrm{MRR}} = 2.36 \times 10^{-11} \mathrm{m^3/s}$, the number of discharges N reaches 3 per 6×10^{-6}s. The following comparative analysis of the simulation results is mainly based on these two bubble generation modes: under low discharge frequency condition, 4 bubbles are generated at random positions in the bottom machining gap per 25 μs; under high discharge frequency condition, 3 bubbles are generated at random positions in the bottom machining gap per 6 μs. The random positions of bubble generation are implemented by UDF.

2.3 Model of debris

Electro erosion debris is thrown out from each electrical discharge position on electrode surface, leading to a complex distribution of initial velocity direction and magnitude. In order to simplify the calculation, the initial velocity of debris v_p is assumed to be 0; that is, only the tractive effect exerted on debris from flow field velocity caused by bubble motion is studied. The numerical range of the spherical debris diameter conforms to the Gaussian function and is set as the Rosin–Rammler distribution: $d_p = 0.5 \sim 0.75 \sim 1 \times 10^{-6}\mathrm{m}$ [20]. The relational expression of the volume of discharge crater V_{crater} and the volume of single debris V_{debris} is $V_{crater} = n \bullet V_{debris}$, where n = 30 is calculated, signifying the number of debris released at one discharge. The debris is set to be released synchronously and randomly with bubbles. The density of workpiece material nickel-chrome alloy steel $\rho_p = 8.4\mathrm{g/cm^3}$ is used and the mass flow rate of debris 1.1e − 7 kg/s is calculated.

The kinematic velocity of debris mainly resulted from the forces exerted by the surrounding fluid [21]:

$$\frac{\mathrm{d}}{\mathrm{dt}}(\mathrm{m_p v_p}) = \mathrm{m_p g} - \rho_\mathrm{m} \mathrm{g} \frac{\mathrm{m_p}}{\rho_\mathrm{p}} + \mathrm{F_{pressure}} + \mathrm{F_{drag}} + \mathrm{F_{saffman}} \tag{11}$$

Equation (11) indicates that the forces exerted on debris consist of two aspects: the gravity and the buoyancy, and the forces exerted by the surrounding fluid: the pressure gradient force $F_{pressure}$, the drag force F_{drag}, and the Saffman lift force $F_{saffman}$, all of which can be configured in DPM-related options combined with UDF settings. Due to the tiny mass of debris, the gravity and the buoyancy are hardly enough for debris to break loose from the forces exerted by the surrounding fluid. As a result, tiny debris tends to follow the flow field streamline to move [22]. The specific formula of the pressure gradient force is

$$F_{pressure} = -\frac{\pi d_p^2}{6} \frac{\partial p}{\partial l} \tag{12}$$

where the term $-\frac{\partial p}{\partial l}$ indicates that $F_{pressure}$ points from the high-pressure region to the low-pressure region in flow field. The aforementioned bubble model regulates that the high-pressure bubbles are only generated in the bottom machining gap, while the side machining gap is connected to the outside atmosphere with much smaller atmospheric pressure. Consequently, $F_{pressure}$ tends to point from the bottom machining gap to the side machining gap entry, which assists in driving the debris to migrate out of the bottom machining gap. The drag force F_{drag} and the Saffman lift force $F_{saffman}$ are related to the velocity difference between debris and fluid:

$$F_{drag}=m_p\frac{18\mu}{\rho_p d_p^2}\left(v-v_p\right) \tag{13}$$

$$F_{saffman}=1.61d_p^2(\rho\mu)^{1/2}\left(v-v_p\right)\left|\frac{\partial v}{\partial l}\right|^{1/2} \tag{14}$$

where F_{drag} and $F_{saffman}$ are both proportional to $v - v_p$. It means that the greater the fluid velocity, the larger the forces exerted on static debris and the easier the debris is dragged to move. The direction of F_{drag} is parallel to the motion direction of debris, which helps debris overcome the viscous resistance of fluid and increase the movement speed. The direction of $F_{saffman}$ is perpendicular to the motion direction of debris, pointing from the low-speed region to the high-speed region in flow field, which controls the steering of debris. The combined action of these multiple forces makes the movement of debris in the flow field quite complicated.

2.4 Boundary condition

The simulation zones are shown in Fig. 1. During the actual machining process, when further increasing the aspect ratio of machined micro-holes, the efficiency and accuracy cannot be maintained, and the problem of the frequent retraction of the tool electrode is inevitable. In order to explore the reason, the simulation geometric model dimension is designed based on the actual machining process of micro-holes with the aspect ratio of 10:1 at the critical depth of 60%. Since the bubbles are only generated in the bottom machining gap, the mesh of the bottom machining gap model is densified with the minimum mesh size as low as 1.5 μm in order to improve the solution accuracy. A certain volume of external flow domain at the side machining gap entry is built, where the motion mode of discrete phase is set to escape, so that the influence of lateral flushing pressure on the fluid movement in machining gap is taken into consideration. The surface roughness Ra of electrodes is set at 0.4 μm for considering the influence of surface recast layer and microcrack that exist in actual machining process on the motion of debris and bubbles, where the motion mode of discrete phase is set to reflect.

The simplified model for calculating the lateral flushing pressure loss when machining micro-holes of high aspect ratio is shown in Fig. 2. The fluid flowing downward along the narrow side machining gap is affected by the viscous resistance τ from the rough inner wall. As a result, the velocity v_f and the pressure p_{flush} of flushing fluid decrease sharply, which is hardly enough to expel the debris from the bottom machining gap. Assuming the flow mode of lateral flushing liquid in the side machining gap as the steady tube flow of incompressible viscous fluid, the pressure drop of the flushing liquid ΔP can be calculated using the Darcy-Weisbach formula [23]:

$$\Delta P=\lambda\frac{l_d}{d_e}\frac{\rho v_f^2}{2} \tag{15}$$

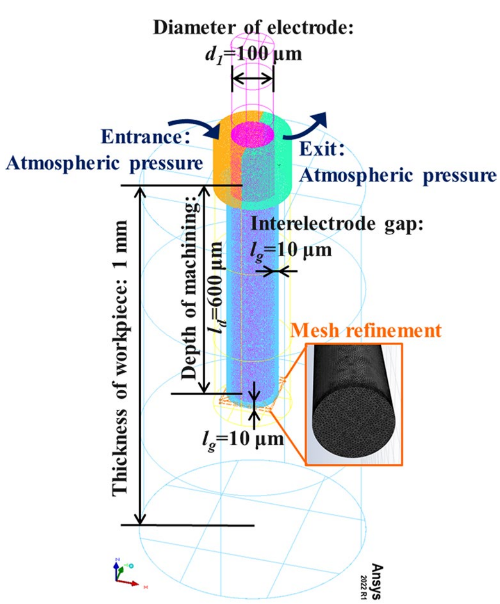

Fig. 1 Geometric model

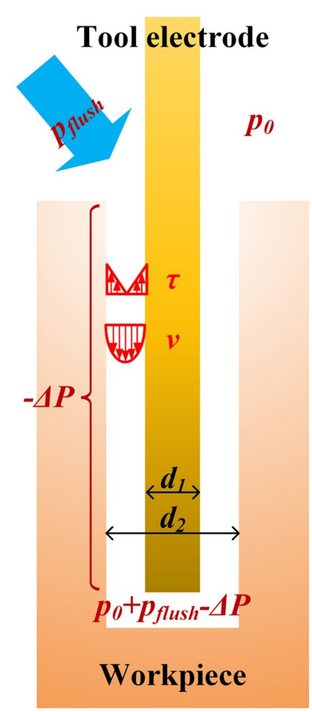

Fig. 2 Lateral flushing pressure loss along machining depth

where the loss coefficient λ of laminar flow along the narrow side machining gap is only related to the Reynolds number: $\lambda = \frac{64}{Re_s}$. When substituting the variables with the actual machining values, such as the lateral flushing speed $v_f = 3m/s$, the gauge pressure drop ΔP is estimated to be 1.44 atm. Compared to the generally used lateral flushing pressure $p_{flush} = 0.2$ atm in micro-EDM, the flushing pressure is too small to compensate for the pressure loss along the narrow gap. The gauge pressure only relying on the lateral flushing technique reaches $p_0 + p_{flush} - \Delta P < 0$, which cannot have any effect on debris expelling. Therefore, other crucial factors dominating the expelling of debris need to be explored. In addition, this model does not include the local pressure loss such as the low-pressure vortex region caused by the sudden contraction of cross-section at the side gap entrance, and the actual total flush pressure loss is greater than the calculation result. Since the lateral flushing pressure has little effect on the debris expelling, also based on the fact that the immersion micro-EDM technique without flushing is feasible, the pressure boundary conditions of the side gap entrance and exit are set to atmospheric pressure, as shown in Fig. 1. Therefore, the interference of the lateral flushing pressure is eliminated, and the crucial factors affecting the debris expelling can be explored.

3 Simulation results and analysis

Without the effects of the lateral flushing pressure and the initially assigned debris motion speed, the debris expelling mainly depends on the action of the high-pressure bubbles. The following sections firstly analyze the kinetic characteristics of bubbles, based on which the mechanism of bubbles on debris expelling and the essence of dielectric fluid cyclic renewal are revealed, providing guidance for future optimization and innovation of processing technologies.

3.1 Kinetic characteristics of bubbles

Figure 3 shows the simulation results of bubble distribution under the low-frequency and high-frequency bubble generation cases respectively. Rather than rising rapidly under the action of buoyancy, the bubbles firstly accumulate in the bottom gap, in which situation the debris is difficult to be driven out of the machining gap. Figure 4 depicts the changing curve of the volume fraction of vapor phase in the machining gap under the low-frequency and high-frequency bubble generation cases respectively. The volume fraction of the vapor phase increases faster under the high-frequency bubble generation case, reaching three times that of low-frequency bubble generation case at

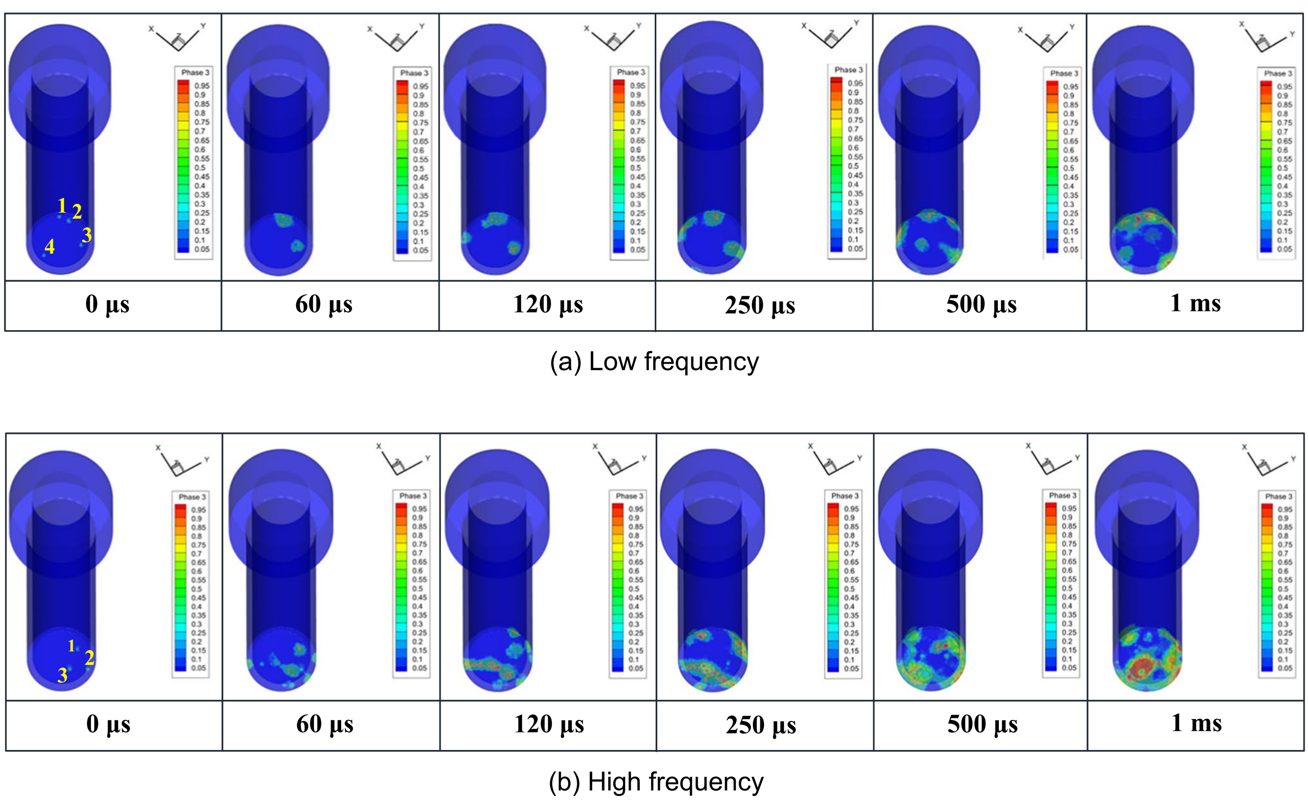

Fig. 3 Cloud diagram of gas phase at different bubble generation frequencies

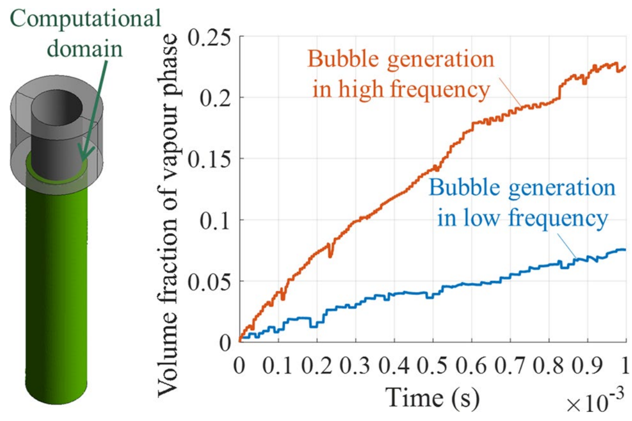

Fig. 4 Volume fraction of vapor phase under different bubble generation frequencies

1 ms, which is consistent with the aforementioned setting of the bubble generation frequency. In addition, the curves in Fig. 4 occasionally fall during the steady rise, indicating the situation of bubble collapsing or condensation [24].

The dimension of narrow micro-EDM machining gap l_g is smaller than the capillary length l_c of the used dielectric fluid: $l_g = 10\mu m < l_c = \sqrt{\frac{\sigma}{\rho g}} = 2.73 \times 10^{-3} m$. Therefore, such scale effect causes the contact liquid film between bubbles and inner wall to produce a large viscous resistance, which counteracts the effect of buoyancy and prevents the bubbles from floating [25], as shown in Fig. 5. This viscous resistance is formed by the disjoining pressure $F_{disjoin}$ and the surface tension F_σ:

$$\frac{d^3 l_f}{dl^3} + \frac{1}{\sigma}\frac{dF_{disjoin}}{dl_f}\frac{dl_f}{dl} = \frac{3\mu v_{up}}{\sigma}\frac{l_f - c}{l_f^3} \tag{16}$$

where the calculated bubble rising speed v_{up} is approaching nanometers per second, that is, almost stagnant [26]. The aforementioned fluid model concerns the effect of surface tension, and the simulation results reflect the influence of viscous resistance on bubbles motion to a certain extent. In summary, the bubbles generated in micro-scale EDM tend to adhere to the inner gap wall surface, firstly gathering in the bottom gap and then gradually accumulating to rise, which is different from the simulation results of large-scale EDM that generated bubbles rapidly float attached with debris out of the machining gap [27].

In order to study the influence of bubble motion on the velocity and pressure of surrounding flow field, five initial bubbles are set to be generated at fixed positions in bottom machining gap, and thus, the interference of random bubble generation in previous model is eliminated to facilitate observation and analysis, as shown in Fig. 6. In the first 100 μs, bubble 1 and bubble 2 in this bubble cluster merged together, while bubbles 3, 4, and 5 experienced the process of expansion and then gradually collapsing and disappearing. In order to analyze the influence of different bubble behavior types on the surrounding fluid, the velocity streamline diagrams of the bottom gap surface at 10 μs and 15 μs are extracted respectively, as shown in Fig. 7. Bubble 3 and bubble 4 gradually shrank during 10 ~ 15 μs with the velocity direction of surrounding fluid radially inward, while bubble 5 continued to expand at 10 μs with the velocity direction of surrounding fluid radially outward and also began to shrink at 15 μs. In other words, the volume of bubbles went through the process of reciprocating oscillation because of the difference between the internal pressure of bubbles and the external pressure of surrounding fluid [28]. As shown in Fig. 8, the initial high pressure assigned to bubbles in the aforementioned model drives bubbles to expand. With the volume of bubbles becoming larger, the internal pressure decreases until it is equal to the pressure of surrounding liquid. Affected by the inertial force exerted from liquid, the bubble boundary will continue to move outward for a certain distance before rebounding, when the internal pressure of bubbles will be less than that of surrounding liquid and the opportunity for bubbles to collapse will be created [29]. The pressure changing curves in Fig. 8 show that the internal pressure of bubble 5 was less than that of surrounding liquid by about 100 Pa at 15 μs when the volume has increased to the maximum. Thereafter, it was compressed to collapse by the surrounding liquid and experienced one

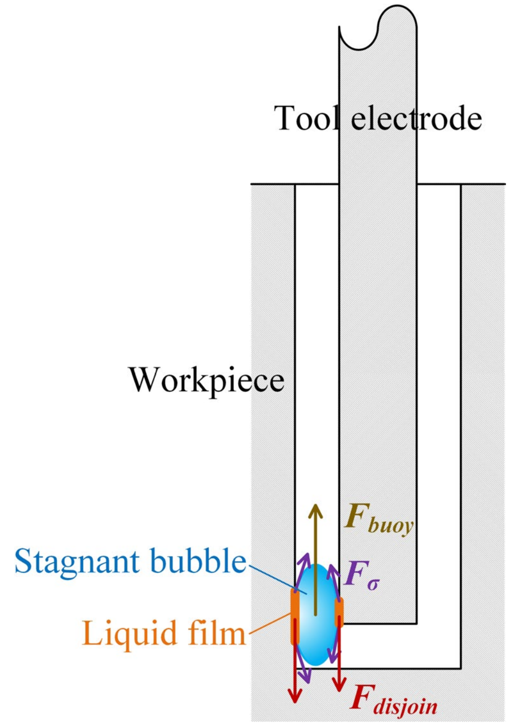

Fig. 5 Force model of bubble stagnation in narrow gap

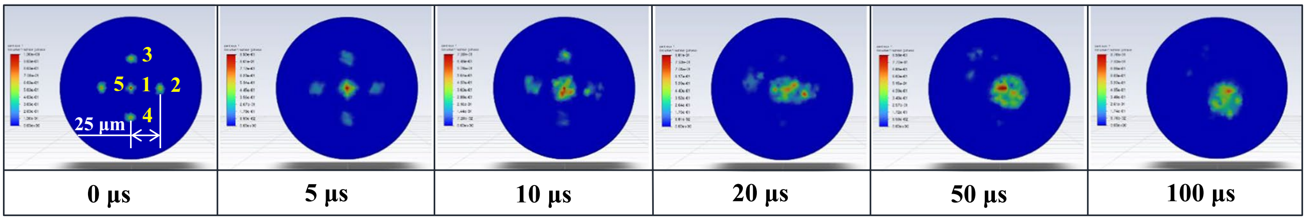

Fig. 6 Evolution process of a bubble cluster at fixed position

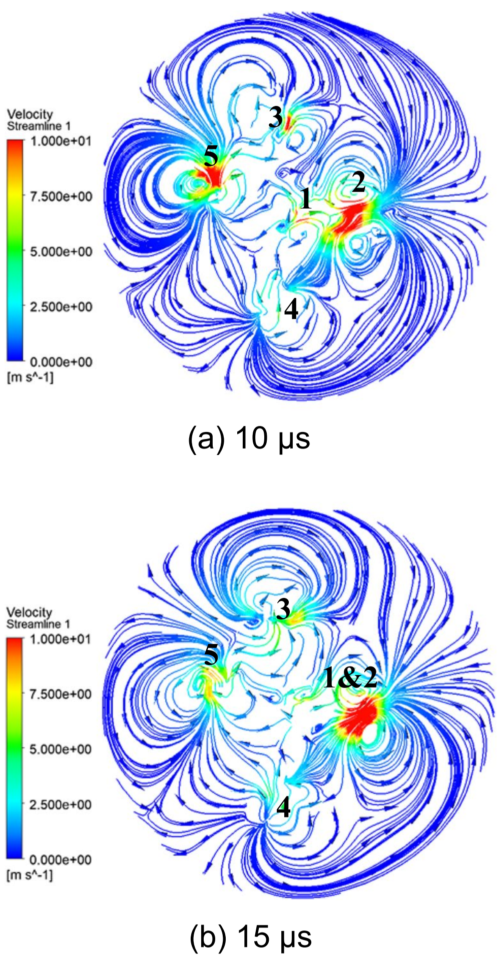

Fig. 7 Streamline diagram of flow field velocity in bottom gap surface at different times

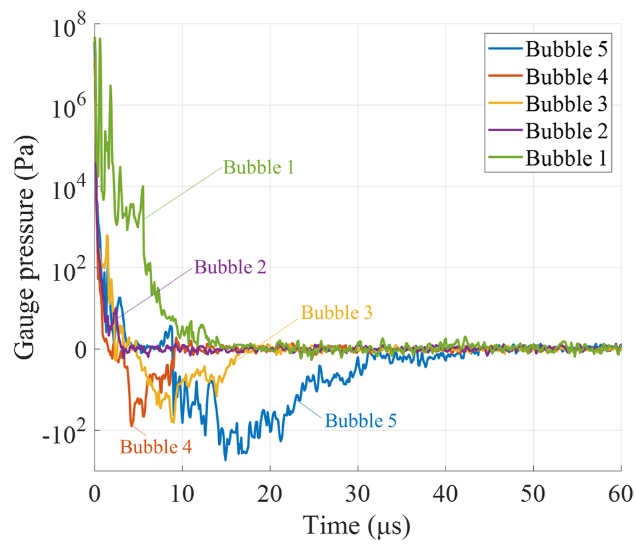

Fig. 8 Changing internal pressure curves of bubbles

oscillation process. By contrast, the internal pressure of bubble 1 and bubble 2 is higher than that of surrounding liquid from beginning to end, and they only undergo the process of expansion and fusion. To verify the simulation results, the simulation parameters of bubble 5: $p_0 - p_q = 100\text{Pa}$, $r_{bi} = 5\mu\text{m}$, are substituted into the Rayleigh-Plesset equation of the spherical bubble dynamics considering viscous force and surface tension [30]:

$$r_b \frac{d^2 r_b}{dt^2} + \frac{3}{2}\left(\frac{dr_b}{dt}\right)^2 + \frac{4\upsilon}{r_b}\frac{dr_b}{dt} + \frac{2\sigma}{\rho r_b} = \frac{p_q - p_0}{\rho} \tag{17}$$

where the solution for the duration time of bubbles from contraction to collapse is $t_c \approx 0.921 r_{\text{bi}} \sqrt{\frac{\rho}{p_0 - p_q}}$. The calculation result and the simulation result of t_c are both several tens of microseconds.

3.2 Effect of bubbles on debris motion

The debris distribution in the machining gap at different bubble generation frequencies is shown in Fig. 9. Since the total number of released debris is quite large, the Tecplot post-processing software is used to only display a fixed percentage of particles for easy observation. Compared with the case of low-frequency bubble generation, although the number of debris increases under high-frequency bubble generation, the debris disperses faster in the bottom gap and rises higher in the side gap, which contributes to improved material removal efficiency. Figure 10 depicts the rising

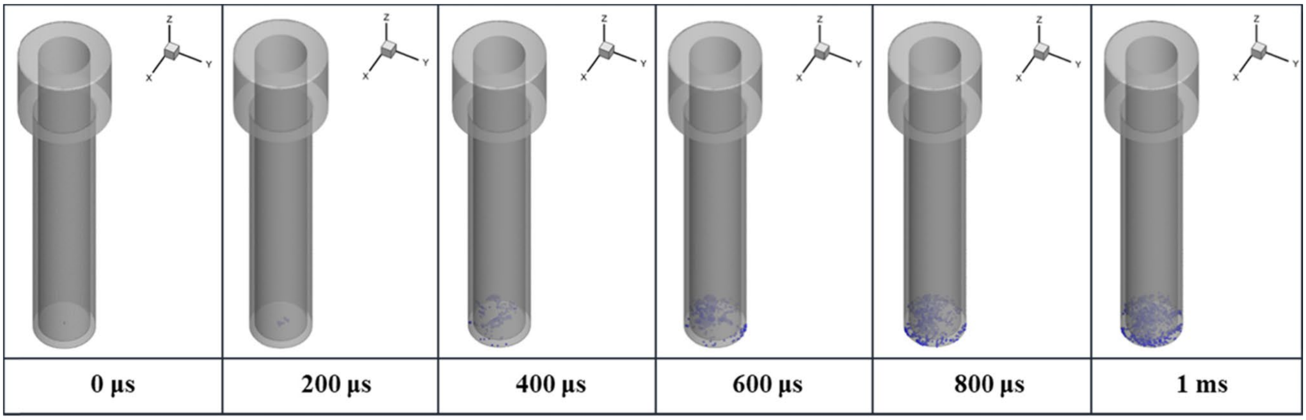

(a) Low frequency

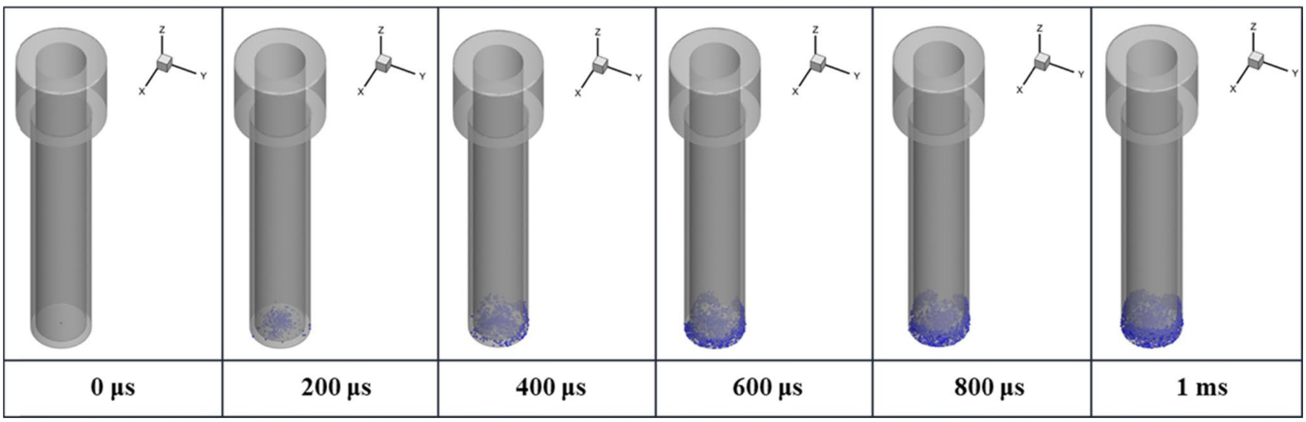

(b) High frequency

Fig. 9 Debris distribution at different bubble generation frequencies

heights of bubbles and debris measured at the same time under different bubble generation frequencies. The rising height of debris at high frequency is higher than that of low frequency, while the rising heights of bubbles have little difference at different frequencies. The changing shape of bubble makes its rising height fluctuate over time. However, the rising height of debris increases almost linearly over time, which is related to the effect of continuously generated high-pressure bubbles on the velocity of surrounding fluid. In addition, regardless of the low-frequency or high-frequency bubble generation conditions, the final rising height of debris is always higher than that of bubbles, as shown in Fig. 11. This indicates that the bubble rising is not the critical factor that drives debris out of the machining gap; other force source affects the debris to move upward preceding the rise of bubbles.

The newly generated high-pressure bubbles will transmit pressure waves to the surrounding liquid when expanding, causing the debris to move away from bubbles, as shown in Fig. 12a. This process is similar to the sudden movement of

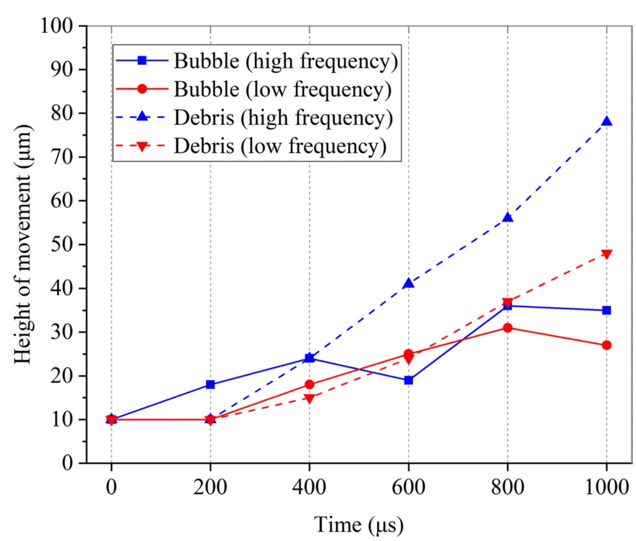

Fig. 10 Rising heights of bubbles and debris under different bubble generation frequencies

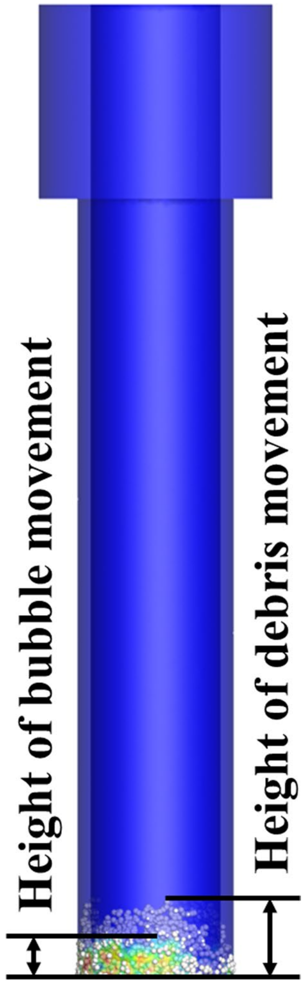

Fig. 11 Vapor and discrete phases under high-frequency bubble generation at 1 ms

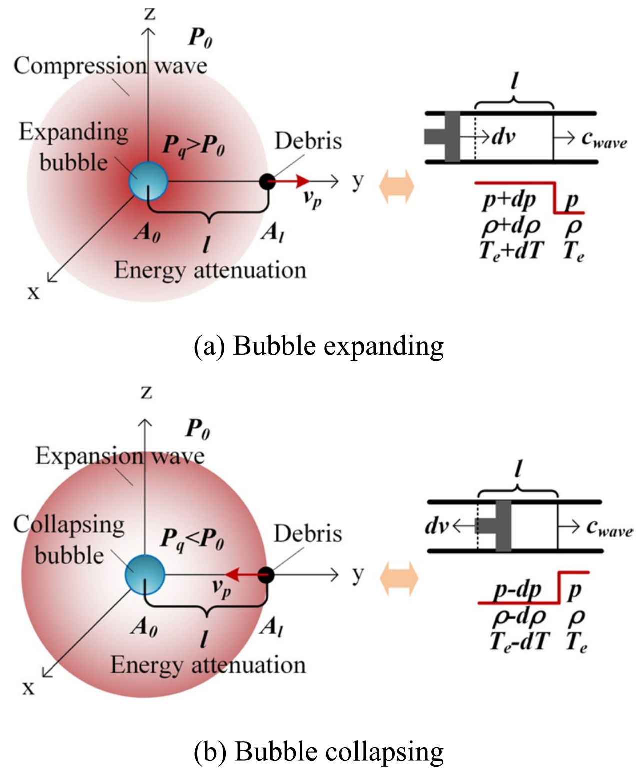

Fig. 12 Effects of bubble motion states on pressure field distribution and debris motion trends in surrounding liquid

the piston in a circular tube at velocity *dv* to the right. The layer of liquid close to the right side of the piston is firstly compressed; then, the liquid is compressed layer by layer and a compressional pressure wave with velocity c_{wave} is formed and spread to the right in turn. Since the aforementioned fluid model sets the liquid phase as compressible, that is, $d\rho \neq 0$, the propagation velocity of pressure waves in liquid phase can be estimated as $c_{wave} = \left(\frac{d\rho}{dp}\right)^{-1/2}$ [14]. After the transmission of pressure waves, the pressure $p + dp$, the density $\rho + d\rho$ and the temperature $T_e + dT$ of surrounding liquid are all higher than that before the transmission. However, due to the energy loss during transmission, the amplitude of pressure waves will be attenuated to $A_l = A_0 e^{-\eta l}$ at distance l from the wave source [31], so that the pressure increment dp cannot be maintained and a pressure gradient field distribution is formed around the high-pressure wave source, as shown in Fig. 12a. The redder the color of fluid around the bubble, the greater the pressure. Based on the aforementioned debris model that the direction of the pressure gradient force exerted by surrounding fluid on debris is from high-pressure region to low-pressure region, the debris tends to move away from bubbles in the flow field under the action of high-pressure compressional waves, which also explains the reasons that only with initial high-pressure bubbles the debris can move from the bottom gap to the side gap in flow field. Therefore, the methods of increasing high-pressure bubbles generation are significant. In addition, Fig. 12b correspondingly describes the rarely occurring situation of the pressure field distribution in surrounding fluid and the movement trend of debris when bubbles collapse, which is similar to the previous analysis process.

The energy of pressure waves will be converted into the kinetic energy of fluid $E_{wave} = \int \frac{(p_q - p_0)^2}{\rho c_l^2} dV$ when propagating in flow field [32]. The liquid will drag the debris to move along the flow field streamline, as shown in Fig. 13. The exponential decay of the pressure wave energy corresponds to the exponential increase of the kinetic energy of fluid, forming a large velocity gradient from the bottom machining gap to the side machining gap in flow field: the maximum velocity in the bottom gap is measured 24.2 m/s, while the minimum velocity in the side gap is measured 0.00836 m/s. This large velocity gradient makes the originally static debris subject to the drag force and the Saffman lift force exerted by surrounding fluid, which play an important role in expelling the debris. When the machining depth increases,

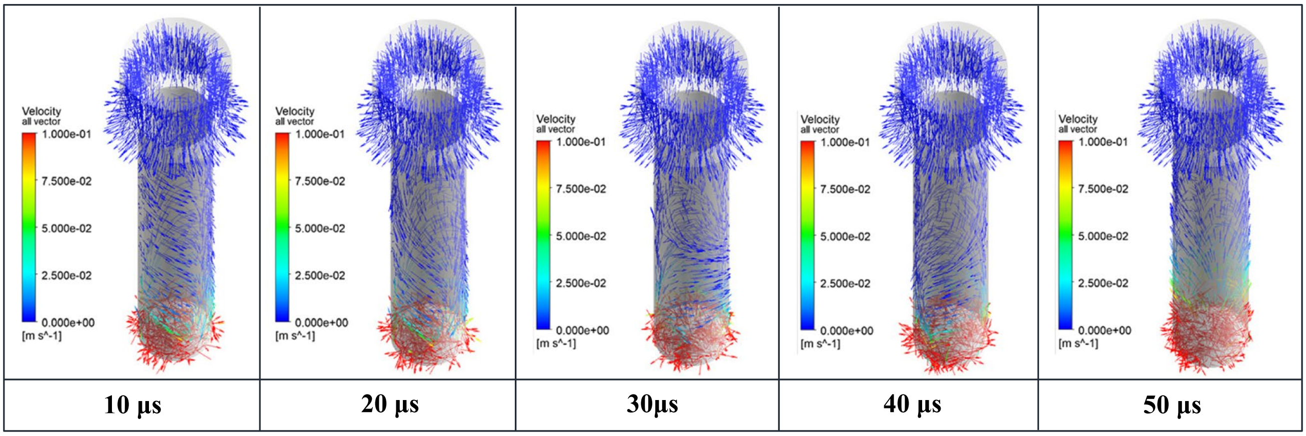

Fig. 13 Vector diagram of flow velocity in machining gap at different times

the flow velocity at side machining gap entry will exponentially decrease, resulting in more and more difficult expelling of debris and decrease in machining efficiency and accuracy. It is foreseeable that high-frequency bubble generation causes more high-pressure bubbles generated, and more pressure wave sources have more pressure wave energy. The fluid obtains greater kinetic energy per unit time, which is easier for debris to be forced out of the machining gap.

At the moment when the high-pressure bubbles are initially generated, the compressional pressure waves emitted to the surrounding flow field greatly increase the kinetic energy of fluid, which cause large fluctuations of flow velocity from the bottom machining gap to the side machining gap entrance. The mass flow rate at the annular plane of the side gap entrance and the average volume pressure at the bottom gap are extracted respectively under different bubble generation frequencies, as shown in Fig. 14, where the positive values of the mass flow rate represent that the fluid flows out of the side gap, while the negative values of the mass flow rate represent that the fluid flows into the side gap. It can be found that every time when high-pressure bubbles are generated, a large fluctuation of the mass flow rate will happen at the side gap entrance, which verifies the correctness of the foregoing analysis. It can also be found that the fluctuation of the mass flow rate slightly lags behind the change of the average pressure. This is because the aforementioned fluid model sets the compressibility of fluid, so that the transmission of pressure waves takes time. However, when the gap fluid is forced by the high pressure from bubbles, it does not necessarily move away from the high-pressure sources and flow out of the gap, or rather; the values of the mass flow rate alternate between positive and negative, forming a dynamic alternation process of flowing into and out of the side machining gap entry. This is because the fluid flow is affected by the machining gap channel structure and the viscous resistance from inner wall, so that the velocity direction

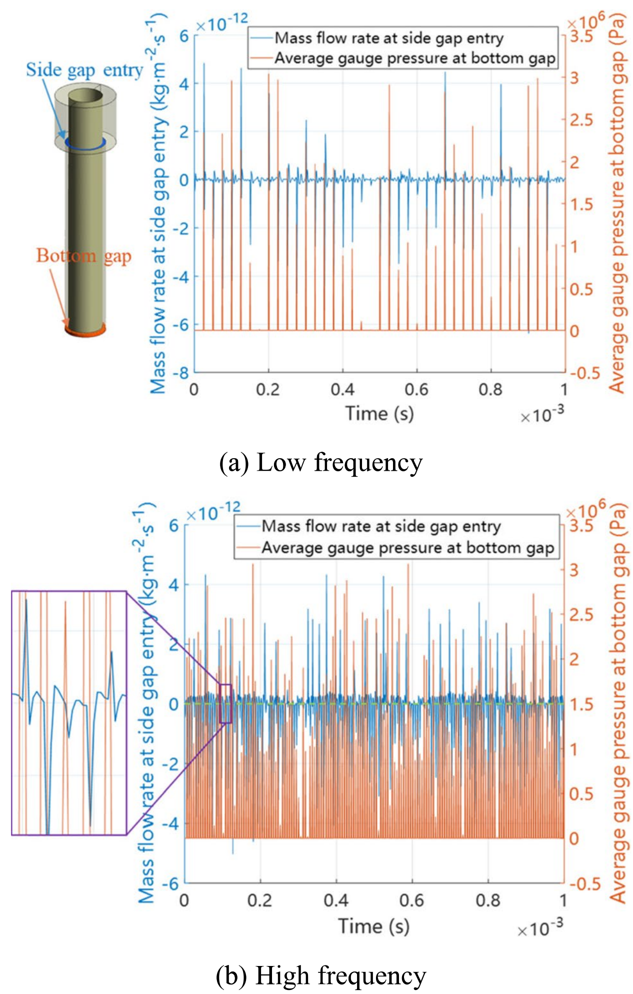

Fig. 14 Variation of mass flow rate at side gap entry corresponding to the average pressure at bottom gap under different bubble generation frequencies

will change during the flow process, as shown in Fig. 13. Although the situation of flowing into the side gap exists, with the continuous accumulation of the gas-phase volume, the gap fluid flows out of the side gap entrance in overall trend; that is, the debris is driven out of the machining gap along the flow field streamline. To verify this point, the mass flow rate within 1 ms is integrated by trapz method, which is calculated as $6.13 \times 10^{-17}\mathrm{kg} \bullet \mathrm{m}^{-2}$ under low-frequency bubble generation and $1.97 \times 10^{-16}\mathrm{kg} \bullet \mathrm{m}^{-2}$ under high-frequency bubble generation respectively. These two positive values demonstrate that the gap fluid flow is net outflow accompanied by alternate inflow, and the efficiency of debris expelling under high-frequency bubble generation is much greater than that under low-frequency bubble generation.

The above simulation results are based on two modes of bubble generation frequencies: the high frequency and the low frequency. In order to explore the influence of bubble generation frequency on the debris expelling efficiency and guide the machining process, the simulation range of the bubble generation frequency is expanded. As shown in Fig. 15, according to the calculation method of bubble generation frequency in the aforementioned bubble model, three new cases of different bubble generation frequencies are simulated, namely, the medium bubble generation frequency signifies 4 bubbles randomly generated every 14 μs, the extra-high bubble generation frequency signifies 3 bubbles randomly generated every 3 μs, and the ultra-high bubble generation frequency signifies 2 bubbles randomly generated every 1 μs. The curve variation trend in Fig. 15 shows that with the continuous increase of the bubble generation frequency, the rising height that debris can reach per unit time is also increasing. This is because the number of high-pressure wave sources becomes larger, which stably maintains the high pressure gradient of the gap flow, increases the kinetic energy of fluid, and obtains a greater mass transfer efficiency. Especially under the ultra-high bubble generation frequency situation, the expelling speed of debris is intrinsically increased, reaching the rising height of 213 μm per ms. This requires that the normal discharge occurs at different positions on workpiece within each microsecond. Therefore, in actual machining process, maintaining interelectrode continuous and stable high-frequency discharge to keep high pressure in bottom gap is of vital

Table 1 Experimental parameters

Parameter	Description
Tool electrode	Cemented carbide (*Φ*100 μm)
Workpiece	18CrNi8 plate (thickness of 1 mm)
Dielectric fluid	Deionized water
Machining polarity	Positive electrode connected to workpiece
Pulsed power modes	Tr-RC, with or without superposition
Open-circuit voltage (V)	140
Pulse width (μs)	2
Pulse interval (μs)	4
Capacitance (nF)	30

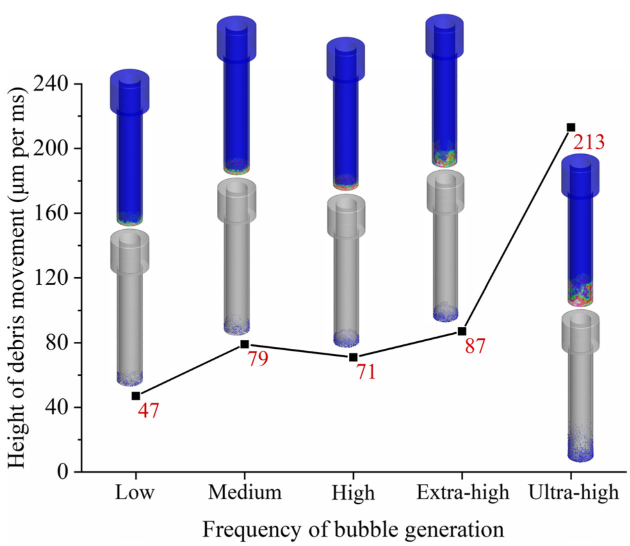

Fig. 15 Final rising heights of debris under different bubble generation frequencies

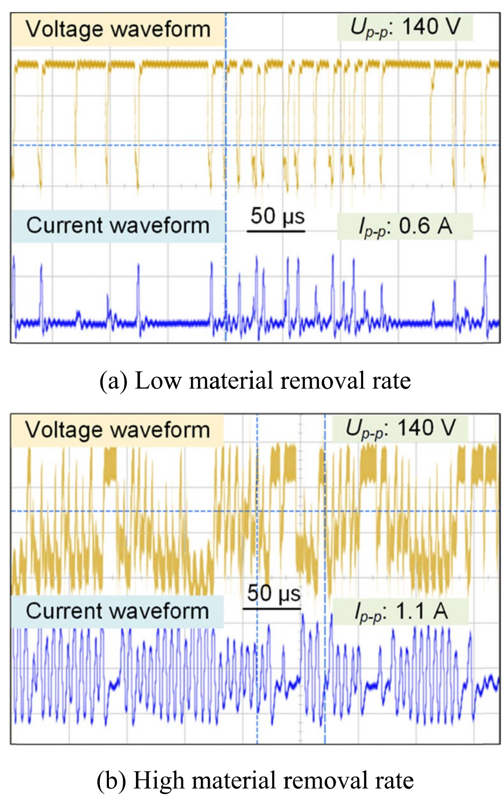

Fig. 16 Discharge waveform of different material removal rates

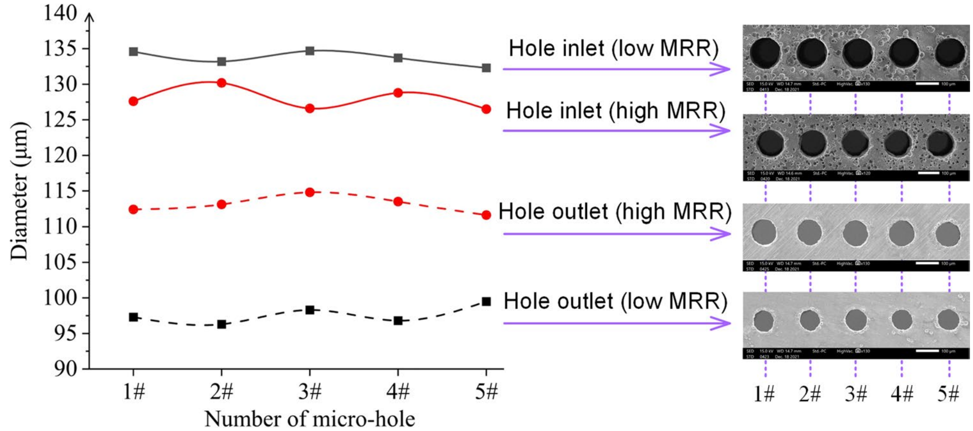

Fig. 17 Micro-hole inlet and outlet of different material removal rates

importance, which necessitates the high effective discharge ratio between electrodes with the pulsed power supply of ultra-high pulse frequency and the optimized interelectrode state detection and servo control strategy, keeping the gap fluid good dielectric properties.

4 Experimental verification

To verify the correctness of the above simulation analysis and conclusions, deep micro-hole EDM experiments were conducted, and the experimental parameters are shown in Table 1. To investigate the effect of bubble generation frequency on machining results, the experimental setup used in the study employed a pulsed power supply with or without superimposed high-frequency oscillation waves to alter the bubble generation frequency [33]. As shown in Fig. 16a, the discharge waveform of the pulsed power supply without superimposed high-frequency oscillation waves had a lower discharge frequency per unit time, resulting in a lower bubble generation frequency and lower material removal rate, which corresponds to the low-efficiency processing conditions described in the previous simulation analysis. In contrast, Fig. 16b shows the discharge waveform of the pulsed power supply with superimposed high-frequency oscillation waves, which had a higher discharge frequency per unit time, resulting in a higher bubble generation frequency and higher material removal rate, corresponding to the high-efficiency processing conditions described in the previous simulation analysis.

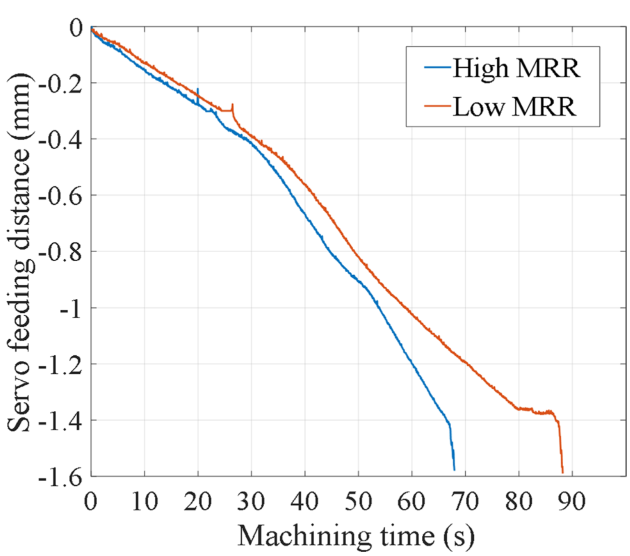

Fig. 18 Servo feeding distances of the *Z*-axis under different material removal rates

The results of micro-holes machining are shown in Fig. 17. The aperture error of multiple micro-holes machined under the same condition is within 5 μm. Under the condition of high MRR, i.e., the condition of high-frequency generation of bubbles, the machining consistency of the inlet and outlet aperture is improved. Figure 18 shows the distance curve of the spindle servo feed in the downward direction. Under the condition of high MRR, i.e., the condition of high-frequency generation of bubbles, the debris expelling circumstance is improved, the phenomenon of obvious spindle retreat caused by gap short-circuit is largely avoided, and the machining stability and efficiency are improved.

5 Conclusions

In order to achieve high-precision and high-efficiency machining of micro-hole with high aspect ratio in micro-EDM and explore the mechanism of interelectrode working fluid renewal and discharge debris expelling, this research established a three-phase flow simulation model of fluid, bubble, and debris in Fluent based on the ideal assumption that bubbles are continuously generated at a set rate in the bottom machining gap. According to the calculation result of the flushing pressure loss along the narrow side machining gap, the boundary condition of the entrance pressure at the side gap is set to 0. Through analyzing the results of simulation and verification experiments, the main conclusions are drawn as follows:

(1) While the high temperature produced from the instantaneous spark discharges gasifies the working fluid to form high-pressure bubbles, the expansion of high-pressure bubble emits compressional wave, which is the source of pneumatic force that drives the working fluid flow at the micron scale, thus promoting the expelling of discharge debris so as to maintain preferable dielectric condition of the working fluid in the machining gap. When the machining depth increases, due to the energy attenuation of the pressure wave propagating from the bottom gap to the side gap inlet, the debris expelling speed and the working fluid renewal efficiency are weakened.
(2) The narrow machining gap in micro-EDM creates the micro-scale effects, resulting in the bubble stagnation caused by the viscous resistance and surface tension of the thin liquid film on the contact gap wall. The generated bubbles firstly gather in the bottom machining gap and then gradually accumulate to rise up. When bubbles are just formed, they expand and emit pressure waves that make the discharge debris move away from the bubbles in the gradient pressure field. While the pressure wave propagates in the flow field, its energy is attenuated and converted into the kinetic energy of the fluid flow, forming a large velocity gradient from the bottom gap to the side gap. Therefore, the discharge debris is dragged by the fluid flow to move away from the bottom gap along the streamline.
(3) Affected by the gap flow channel structure and the viscous resistance from inner wall, the moving direction of the discharge debris in the flow field changes, forming a dynamic alternation process of flowing into and out of the side machining gap entry. Due to the continuous accumulation of the gas-phase volume, the discharge debris is expelled out of the side gap entrance in overall trend.
(4) The bubble generation frequency is a key factor affecting the debris expelling efficiency. When the bubble generation frequency is increased to the megahertz level, the debris expelling efficiency has a step-like improvement. Under the set bubble generation frequency, since it is assumed that the high-pressure bubbles are generated constantly and uninterruptedly, the high pressure gradient in the machining gap is ensured to be maintained. Therefore, the discharge debris is able to continuously move upward without falling back to accumulate in the bottom gap, which is beneficial to the stable and smooth machining process.

This research reveals the flow behavior of the working fluid in the micro-EDM gap. It is undoubtedly that the key to smoothly machine the micro-holes with high aspect ratio by micro-EDM is to keep the high-pressure bubbles continuously generated at high frequency and promote the inflow of fresh working fluid and the outflow of discharge debris. This has laid a theoretical foundation and clarified a feasible technical approach for us to further optimize the interelectrode gap servo control, improve the effective discharge ratio, and achieve high-precision and high-efficiency machining of micro-holes with high aspect ratio.

Nomenclature A_0: Initial amplitude of pressure wave, m; A_l: Amplitude of pressure wave after propagation distance l, m; A_S: Flow area of side machining gap cross-section, μm^2; c: Constant; c_1: Sound velocity of liquid phase, m/s; c_{wave}: Transmission velocity of pressure wave in liquid, m/s; d_1: Diameter of tool electrode, μm; d_2: Diameter of machined micro-hole, μm; dp: Change of fluid pressure, Pa; dT: Change of fluid temperature, K; dv: Change of fluid velocity, m/s; dV: Symbol of volume integral; dρ: Change of fluid density, kg/m^3; d_p: Diameter of debris, μm; d_e: Equivalent diameter of side machining gap cross-section, μm; E_e: Energy in the energy equation, J; E_{wave}: Energy of pressure waves, J; F_{buoy}: Buoyancy on bubbles, N; F_{disjoin}: Disjoining pressure between bubble and contact wall, N; F_{drag}: Drag force exerted on debris by surrounding fluid, N; F_{pressure}: Pressure gradient force exerted on debris by surrounding fluid, N; F_{saffman}: Saffman lift force exerted on debris by surrounding fluid, N; F_σ: Surface tension of the fluid, N; g: Gravitational acceleration, m/s^2; h_v: Heat of vaporization, kJ/kg; $I(t)$: Discharge current, A; K_{qp}: Factor of phase transition intensity; K_{eff}: Effective thermal conductivity coefficient in energy equation; k_G: Gaussian heat coefficient; L_e: Latent heat of vaporization, kJ/kg; l: Distance between any two points in machining gap, μm; l_c: Capillary length of the dielectric fluid, m; l_d: Machining depth of micro-holes, mm; l_f: Liquid film thickness between bubbles and contact wall, nm; l_g: Machining gap width, μm; m_p: Mass of debris, kg; $\dot{\text{m}}_{\text{pq}}$: Mass transfer velocity from liquid phase to gas phase, kg/s; $\dot{\text{m}}_{\text{qp}}$: Mass transfer velocity from gas phase to liquid phase, kg/s; N: Number of initial generated bubbles; n: Number of particles released at one time; n_v: Unit normal vector of fluid interface; p: Shared pressure of fluid phase, Pa; p_0: Atmospheric pressure, Pa; p_{flush}: Lateral flushing pressure, Pa; p_q: Pressure of gas phase, Pa; p_{sat}: Saturated vapor pressure, Pa; $q(r,t)$: Gaussian heat, J; Re_b: Fluid Reynolds number in bottom machining gap; Re_s: Fluid Reynolds number in side machining gap; $R(t)$: Discharge channel radius, μm; r: Distance from discharge center, μm; r_b: Bubble radius, μm; r_{bi}: Initial bubble radius, μm; $\text{S}_{\text{a}_\text{q}}$: Source term in Continuity Equation, kg/m^3-s; S_h: Source term in Energy Equation, W/m^3; T_e: Temperature in Energy Equation, K; T_{nuc}: Nucleation temperature, K; T_{sat}: Saturated temperature, K; t_c: Time of bubble collapse, μs; t_{on}: Pulse width of the pulsed power supply, μs; t_{total}: Total time of micro-hole machining, s; $U(t)$: Discharge voltage, V; V_c: Volume of single grid cell, μm^3; V_{crater}: Volume of single discharge crater, μm^3; V_{debris}: Volume of single debris, μm^3; $\text{V}_\text{f}^{\text{n+1}}$: Volumetric flux on surface through normal velocity vector at $n+1$ time step, m^3/s; V_{total}: Total volume of removed workpiece material, m^3; v: Shared velocity of fluid phase, m/s; v_b: Initial expansion velocity of bubbles, m/s; v_f: Lateral flushing speed, m/s; v_p: Movement velocity of debris, m/s; v_q: Movement velocity of gas interface, m/s; v_s: Fluid flow speed in side machining gap, m/s; v_{up}: Rising speed of bubbles in narrow gap, nm/s; α_q: Volume fraction of gas phase; α_q^n: Volume fraction of gas phase at n time step; $\alpha_\text{q}^{\text{n+1}}$: Volume fraction of gas phase at $n+1$ time step; ΔP: Pressure loss along the side gap channel, Pa; Δt: Unit of time, s; ΔV: Material removal volume per unit time, m^3; η: Pressure wave energy attenuation coefficient; η_G: Gaussian heat transfer coefficient; κ: Surface curvature, m^{-1}; λ: Pressure loss coefficient along the side gap channel; μ: Dynamic viscosity of fluid, Pa·s; ρ: Shared density of fluid phase, kg/m^3; ρ_p: Density of debris, kg/m^3; ρ_q: Density of gas phase, kg/m^3; ρ_q^n: Gas-phase density at n time step, kg/m^3; ρ_q^{n+1}: Gas-phase density at $n+1$ time step, kg/m^3; σ: Surface tension coefficient of fluid, N/m; τ: Tangential stress, Pa; υ: Kinematic viscosity of fluid, m^2/s; χ: Wet perimeter of side machining gap, μm

Funding This research was supported by the National Natural Science Foundation of China (grant No. 92060108) and Independent Research Project of State Key Laboratory of Tribology of China (grant No. SKLT2022B08).

Declarations

Ethics approval The authors declare that no animals or human participants are involved in this research.

Competing interests The authors declare no competing interests.

References

1. Chen Y, Chen, MY (2020) Fabrication of vertical through-holes to realize high throughput cell counting. IEEE Electron Packag Technol Conf, EPTC 189–193. https://doi.org/10.1109/EPTC50525.2020.9315101
2. Adrija B, Shibendu SR (2021) A review on multi nozzle electrohydrodynamic inkjet printing system for MEMS applications. IOP Conf Ser: Mater Sci Eng 1136:012015. https://doi.org/10.1088/1757-899X/1136/1/012015
3. Kumar R, Singh I (2021) Blind hole fabrication in aerospace material Ti6Al4V using electric discharge drilling: a tool design approach. J Mater Eng Perform 30:8677–8685. https://doi.org/10.1007/s11665-021-06052-0
4. Tong H, Li Y, Zhang L, Li BQ (2013) Mechanism design and process control of micro EDM for drilling spray holes of diesel injector nozzles. Precis Eng 37:213–221. https://doi.org/10.1016/j.precisioneng.2012.09.004
5. Feng GL, Yang XD, Chi GX (2019) Experimental and simulation study on micro hole machining in EDM with high-speed tool electrode rotation. Int J Adv Manuf Technol 101:367–375. https://doi.org/10.1007/s00170-018-2917-6
6. Li ZK, Bai JC (2018) Influence of alternating side gap on microhole machining performances in micro-EDM. Int J Adv Manuf Technol 94:979–989. https://doi.org/10.1007/s00170-017-0959-9
7. Tong H, Li Y, Wang Y (2008) Experimental research on vibration assisted EDM of micro-structures with non-circular cross-section. J Mater Process Technol 208:289–298. https://doi.org/10.1016/j.jmatprotec.2007.12.126
8. Li GD, Natsu W (2020) Realization of micro EDM drilling with high machining speed and accuracy by using mist deionized water jet. Precis Eng 61:136–146. https://doi.org/10.1016/j.precisioneng.2019.09.016
9. Liao Y, Liang HW (2016) Study of vibration assisted inclined feed micro-EDM drilling. Proc CIRP 42:552–556. https://doi.org/10.1016/j.procir.2016.02.250
10. Li Y, Hu RQ (2013) Size and profile measurement of micro holes by mold extraction and image processing. Nano Technol Precis Eng 11(4):341–347. https://doi.org/10.13494/j.npe.2013.057. ([in Chinese])
11. Li GD, Natsua W, Yu ZY (2019) Study on quantitative estimation of bubble behavior in micro hole drilling with EDM. Int J Mach Tool Manuf 146:103437. https://doi.org/10.1016/j.ijmachtools.2019.103437
12. Yin QF, Wu PY, Qian ZQ, Zhou L, Shi W, Zhong L (2020) Electrical discharge drilling assisted with bubbles produced by electrochemical reaction. Int J Adv Manuf Technol 109:919–928. https://doi.org/10.1007/s00170-020-05709-9
13. Hirt CW, Nichols BD (1981) Volume of fluid (VOF) method for the dynamics of free boundaries. J Comput Phys 39(1):201–225. https://doi.org/10.1016/0021-9991(81)90145-5
14. Shaw SJ, Spelt PDM (2010) Shock emission from collapsing gas bubbles. J Fluid Mech 646:363–373. https://doi.org/10.1017/S0022112009993338
15. Ikeda M (1972) The movement of a bubble in the gap depending on the single electrical discharge I. J Jpn Soc Electr Mach Eng 6(11):12–26. https://doi.org/10.2526/jseme.6.12
16. Shao B, Rajurkar KP (2015) Modelling of the crater formation in micro-EDM. Proc CIRP 33:376–381. https://doi.org/10.1016/j.procir.2015.06.085
17. Irvine TF, Harnett JP (1978) Advances in heat transfer. Stony Brook, New York.https://doi.org/10.1016/B978-0-12-020051-1.50001-2
18. Shervani TMT, Abdullah A, Shabgard MR (2006) Numerical study on the dynamics of an electrical discharge generated bubble in EDM. Eng Anal Bound Elem 30:503–514. https://doi.org/10.1016/j.enganabound.2006.01.014
19. Kojima A, Natsu W, Kunieda M (2008) Spectroscopic measurement of arc plasma diameter in EDM. CIRP Ann-Manuf Techn 57(1):203–207. https://doi.org/10.1016/j.cirp.2008.03.097
20. Mastud SA, Kothari NS, Singh RK, Joshi SS (2015) Modeling debris motion in vibration assisted reverse micro electrical discharge machining process (R-MEDM). J Microelectromech Syst 24(3):661–676. https://doi.org/10.1109/JMEMS.2014.2343227
21. Loth E, Dorgan AJ (2009) An equation of motion for particles of finite Reynolds number and size. Environ Fluid Mech 9:187–206. https://doi.org/10.1007/s10652-009-9123-x
22. Peng ZB, Ge LH, Moreno-Atanasio R, Evans G, Moghtaderi B, Doroodchi E (2020) VOF-DEM study of solid distribution characteristics in slurry Taylor flow-based multiphase microreactors. Chem Eng J 396:124738. https://doi.org/10.1016/j.cej.2020.124738
23. Massey BS (1989) Mechanics of Fluids. Van Nostrand Reinhold, New York
24. Tiwari A, Pantano C, Freund JB (2015) Growth-and-collapse dynamics of small bubble clusters near a wall. J Fluid Mech 775:1–23. https://doi.org/10.1017/jfm.2015.287
25. Bretherton F (1961) The motion of long bubbles in tubes. J Fluid Mech 10(2):166–188. https://doi.org/10.1017/S0022112061000160
26. Dhaouadi W, Kolinski JM (2019) Bretherton's buoyant bubble. Phys Rev Fluids 4(12). https://doi.org/10.1103/PhysRevFluids.4.123601
27. Wang J, Han FZ (2014) Simulation model of debris and bubble movement in consecutive-pulse discharge of electrical discharge machining. Int J Mach Tool Manuf 77:56–65. https://doi.org/10.1016/j.ijmachtools.2013.10.007
28. Lauterborn W, Kurz T (2010) Physics of bubble oscillations. Rep Prog Phys 73(10). https://doi.org/10.1088/0034-4885/73/10/106501
29. Rayleigh L (1917) On the pressure developed in a liquid during the collapse of a spherical cavity. Phil Mag 34:94–98. https://doi.org/10.1080/14786440808635681
30. Plesset MS (1949) The dynamics of cavitation bubbles. ASME J Appl Mech 16:277–282
31. Huang F, Bai BF, Guo LJ (2004) A mathematical model and numerical simulation of pressure wave in horizontal gas-liquid bubbly flow. Prog Nat Sci 14:344–349. https://doi.org/10.1080/10020070412331343591

32. Fortes-Patella R, Challier G, Reboud JL, Archer A (2013) Energy balance in cavitation erosion: from bubble collapse to indentation of material surface. ASME J Fluids Eng 135(1):011303. https://doi.org/10.1115/1.4023076
33. Cao PY, Tong H, Li Y (2022) Pulsed power supply superposed with radio frequency oscillating wave for the improvement of micro-electrical discharge machining process. ASME J Micro Nano-Manuf 10(1):011004. https://doi.org/10.1115/1.4054974